Structural rearrangements during sub-T_g relaxation and nucleation in lithium disilicate glass revealed by a solid-state NMR and MD strategy

Henrik Bradtmüller[1,*], Anuraag Gaddam[2], Hellmut Eckert[2], Edgar D. Zanotto[1]

[1]Department of Materials Engineering, Vitreous Materials Laboratory, Federal University of São Carlos, CP 676, 13565-905, São Carlos, SP, Brazil
[2]São Carlos Institute of Physics, University of São Paulo, Avenida Trabalhador Sãocarlense 400, São Carlos, 13566-590, SP, Brazil

ABSTRACT: Structural rearrangements taking place during relaxation and crystal nucleation in lithium-disilicate (LS2) glass have been investigated by a comprehensive set of solid-state nuclear magnetic resonance (NMR) experiments, supported by molecular dynamics (MD) simulations. Samples were subjected to heat treatments at 435 °C, i.e., 20 K below the laboratory glass transition temperature (T_g). Raman and NMR data indicate that under these conditions both relaxation and nucleation occur without detectable changes in the network former unit distribution of the glassy silicon-oxide network. Instead, relaxation of the frozen supercooled melt and nucleation of LS2 crystals occur principally in terms of a changing lithium local environment: ^{7}Li spin-echo decay NMR indicates average Li-Li distances, characterized by homonuclear dipolar second-moment measurements, are reduced after very short heat treatments and approach those found in the isochemical crystal. This finding is supported by molecular dynamics (MD) simulations predicting a dependence of the Li^+ ion distribution on the melt-cooling rate. In addition, the structural reorganization also impacts the distribution of electric field gradients as detected by ^{7}Li satellite transition NMR spectroscopy. Finally, crystal nucleation becomes most evident by the appearance of minor amounts of sharp ^{29}Si MAS resonances and a significant change in the ^{7}Li NMR satellite transitions, as visualized by difference spectroscopy. This study defines a new NMR strategy, generally applicable for investigating the structural relaxation process accompanying the internal crystallization of ion-conducting frozen supercooled melts containing suitable NMR active nuclear probes (^{7}Li, ^{23}Na, ^{133}Cs, etc.).

KEYWORDS: relaxation, nucleation, lithium disilicate, solid state NMR, MD simulation

(*) Corresponding author: H. Bradtmüller

E-mail: mail@bradtmueller.net. Phone: +55-16-33518556. Fax: +55-16-33615404.

Address: Department of Materials Engineering, Federal University of São Carlos, Rod. Washington Luis, km 235 C.P. 676 13.565-905 - São Carlos / SP – Brazil

1. Introduction

According to contemporary understanding, glasses are non-crystalline substances, which normally originate from the freezing of supercooled liquids (SCLs). They are non-equilibrium states and their structures are quite similar to those of their isochemical SCLs. [1-4] This implies, that state functions such as molar volume, enthalpy, and entropy depend on the cooling rate with which the glasses are prepared, which is well-confirmed by experimental evidence. Likewise, it is known that the microstructure and macroscopic properties of the glass-ceramics prepared from them are greatly dependent on the annealing protocols applied. The situation is illustrated in Figure 1. Kinetic inhibition maintains the supercooled liquid state below the freezing point, T_m, and the state functions continue to decrease monotonically with decreasing temperature as long as the system can respond sufficiently rapidly to the change in temperature by adjusting its molecular/atomic structure. However, as the temperature keeps decreasing, molecular motion keeps slowing down, until the system ultimately reaches the characteristic glass transition region where the experimental time scale exceeds the rate of molecular relaxation and the SCL temporarily freezes into a glass. In this regime, molecular/structural adjustment towards the stationary supercooled liquid or, ultimately, to the thermodynamically favored crystalline state can no longer be observed unless one waits for some extra time. The temperature where this phenomenon takes place on the cooling path is known as the *fictive temperature*, T_f, and manifests itself by a change of slope, dX/dT, of any observable property X. In most practical cases, however, one measures a related temperature, known as the glass transition temperature, T_g, in heating experiments. The actual value of T_g depends on the chemical composition, the observable, and the rate with which it is being monitored, as well as the thermal history of the glass under investigation (which was frozen at T_f). The most common observables are the heat capacity (indirectly measured via differential scanning calorimetry), the viscosity, and the thermal expansion coefficient. The temporarily frozen supercooled liquid (glass) can be transformed back into the stationary supercooled liquid by extended thermal annealing (measurable at temperatures 5 to 50 °C below T_g). This process is called "*relaxation*" and results in a reduction in the fictive temperature, T_f. In parallel to this process, random structural fluctuations can lead to the formation of crystalline nuclei, which, once the latter exceed a certain critical size, can spontaneously grow via diffusion-limited mass transport resulting in the formation of glass-ceramics.

The pathway from the vitreous state towards the SCL state and, finally, crystallization remains microscopically ill-understood. Since possible structural changes of glass during its relaxation, nucleation and crystallization occur on atomic length scales, conventional materials characterization methods like powder X-Ray diffraction, microscopies, and even vibrational and nuclear magnetic

resonance spectroscopies are commonly pushing their limits. A case in point are numerous solid-state NMR and Raman studies published on the crystallization of lithium disilicate glass.[5-14]. While both methods can easily differentiate between crystalline and glassy LS2 and are thus suitable for monitoring crystallization, they lack the ability to reveal further details on the microstructural organization of the glasses as they relax towards the supercooled liquid state and/or undergo crystal nucleation. An exception is observed for glasses with "off-stoichiometric" compositions, where the initial crystallizing phase is lithium metasilicate, and ^{29}Si magic-angle spinning NMR can reveal the higher degree of polymerization of the glassy phase that remains behind [5]. However, in all of those cases where crystallization proceeds directly via homogeneous nucleation of stoichiometric $Li_2Si_2O_5$, neither NMR nor vibrational spectroscopy has given much information. As glassy lithium disilicate contains about 75% Q^3 and 12.5% of Q^4 and Q^2 units, their final conversion to all-Q^3 lithium disilicate (upon full crystallization) has to invoke the equilibrium

$$2Q^3 \leftrightarrow Q^4 + Q^2 \qquad (1)$$

On the other hand, such equilibration in glasses at or below T_g can take many hours or days. For instance, Soares Jr et al. [15] studied the early and intermediate stages of crystallization of hypo-, hyper- and stoichiometric lithium disilicate glasses heat-treated at T_g = 454 °C for 2.5 to 600 h (~35 vol.% crystallized fraction). Transmission Electron Microscopy (TEM) analyses of specimens provided clear evidence of a second phase, viz. lithium metasilicate (LS), which nucleates simultaneously with the stable LS2 phase. The LS/LS2 ratio decreased with heat treatment time up to 120 h (< 1% volume fraction crystallized) after which the LS crystals, which likely form during the cooling path of the melt or heating procedure to the nucleation temperature (454 °C in this case), dissolved back into the SCL. They likely form during the cooling path of the melt or heating procedure to the nucleation temperature (454 °C in this case). However, so far, no convincing evidence by NMR or Raman spectroscopy has ever been presented suggesting Q^n speciation changes effected by sub-T_g annealing, perhaps because nobody has performed the required long thermal treatments.

In contrast to the silicate network, the lithium ions are highly mobile in this temperature region [16] and could easily respond with regard to their structural re-arrangement upon relaxation and nucleation. Based on these considerations, the present study focuses on changes in the structural features of the lithium oxide network modifier during the relaxation process. Such information is readily available from an analysis of the internal magnetic and electric interactions affecting ^{7}Li nuclear precession frequencies in solid-state NMR experiments. They comprise (a) the magnetic shielding effects exerted by the core and valence electrons surrounding the nuclei, (b) the local

magnetic fields produced by other nuclear magnetic moments (in the present case dominantly other ^{7}Li nuclei) in the vicinity of the probe nucleus, and (c) the interactions between the ^{7}Li nuclear electric quadrupole moments and the electric field gradients characterizing the charge/electron density distribution produced by the local oxygen coordination of the lithium species. Based on the above considerations, the present study focuses on the structural properties of the lithium ions in lithium disilicate glass and their modifications caused by relaxation and nucleation upon thermal annealing below the glass transition temperature. Using a combination of various static and MAS ^{7}Li solid-state NMR methods, here we develop and test a new solid-state NMR strategy that can be generalized to the study of other supercooled liquids.

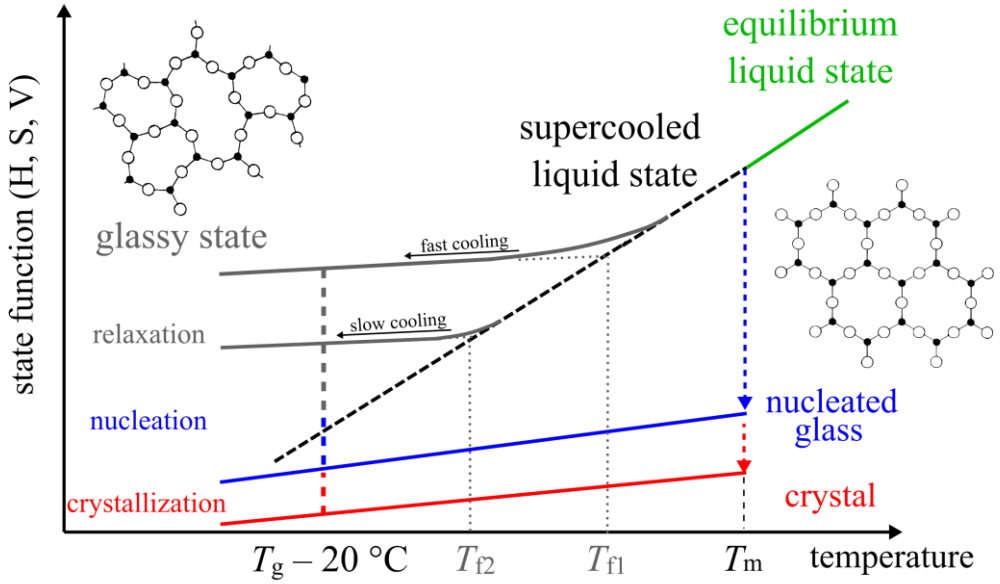

Figure 1: Property (enthalpy *H*, entropy *S*, or volume *V*) temperature diagram for a slowly cooled and a fast cooled SCL. The glass transition temperature, T_g, is typically detected in heating experiments between T_{f1} and T_{f2}.

2. Materials and Methods

2.1 Sample Preparation and Characterization

Lithium disilicate glass was synthesized by mixing fine dried Li_2CO_3 (Sigma, 99.0%) powder and SiO_2 (Zetasil 02, 99.9%) in a Li/Si molar ratio of 1:1, and homogenizing the mixture in a rotary jar mill for 18 h. The mixture was placed in a platinum crucible, repeatedly melted in a high-temperature furnace at 1400°C for 3 h, and subsequently, cast and splat cooled on a room temperature copper plate for a total of three times. The obtained colorless and visually homogeneous glass was stored in a dry atmosphere. For the thermal treatments, the glass was cut into pieces of approximately 2 g and placed in a vertical furnace operating at a temperature of 435 °C (~T_g – 20 °C). At designated times ranging

from 15 min to 60 d, individual samples were removed from the furnace and allowed to cool quickly under ambient conditions. Finally, the treated samples were stored in a dry atmosphere. Part of the as-quenched glass was subjected to a crystallization heat treatment at 645 °C for 4 h to produce a specimen of fully crystalline $Li_2Si_2O_5$ used as reference compound.

The identity of the produced $Li_2Si_2O_5$ specimen and possible crystalline phases in the heat treated LS2 glasses were confirmed by X-ray diffraction, using a Rigaku Ultima IV diffractometer with Cu target (K_α wavelength) operating at 40 kV and 20 mA. The 10° to 80° 2θ range was probed at room temperature employing an integration time of 2.5 s and a step size of 0.02°. Results are shown in Figure S1 of the Supporting Information.

Characteristic temperatures were determined by Differential Scanning Calorimetry (DSC) on a Netzsch DSC 404 cell equipped with a TASC 414/3 controller using monolithic pieces of approximately 15 – 20 mg with at heating rates of 10 K/min. Raman spectra were measured in the 200 – 1325 cm^{-1} range with an acquisition integration time of 100 s and 2 cycles using a LabRAM HR 800 Raman spectrophotometer (Horiba Jobin Yvon) equipped with a CCD detector (model DU420A-OE-325) and a He–Ne laser (632.81 nm).

2.2 MD Simulations

Molecular dynamics simulations were performed using the Large-scale Atomic/Molecular Massively Parallel Simulator (LAMMPS) software package. [17, 18] For all simulations, rigid body potentials developed by Pedone et al. [19] were used, consisting of (a) long-range Coulomb potential, (b) short-range Morse function, and (c) repulsive contribution $1/r^{12}$, given by,

$$U(r) = \frac{z_i z_j e^2}{r} + D_{ij}\left\{\left(1 - e^{-a_{ij}(r-r_0)}\right)^2 - 1\right\} + \frac{C_{ij}}{r^{12}} \qquad (2)$$

The potential parameters for the Li-O, Si-O, and O-O atomic pairs interactions are presented in Table 1. The long-range Coulomb interactions were evaluated using the Ewald summation [20] with a precision of 10^{-5} in force and a cutoff of 12 Å. The integration of Newton's equations of motions was conducted using the velocity Verlet algorithm with a simulation timestep of 1 fs. The temperature and pressure were controlled using a Nosé–Hoover thermostat and a barostat at every 100 steps.[21, 22] In all the simulations periodic boundary conditions were used on three axes. A total of 10,200 atoms were simulated that were initially randomly generated in a cubic simulation box of dimensions corresponding to the experimental density of the LS_2 glass. The obtained structure was first minimized for energy. Then the glasses were heated from 300 to 5000 K at a rate of 100 K ps^{-1}

using NVT ensemble. The samples were held at the fusion temperature of 5,000K for 100 ps under NVT ensemble. Then the samples were quenched to 300 K under NVT conditions at rates of 1, 10, 100, 1,000, 10,000 K ps^{-1} and were then thermalized at 300 K for 100 ps at constant volume conditions followed by another 100 ps under constant pressure conditions. Each quenching rate was repeated three times for averaging purposes. The obtained final structures were analyzed using a laboratory-developed code to calculate radial distribution functions (see Figure S2), ^{7}Li-^{7}Li dipole-dipole second moments ($M_{2\mathrm{Li-Li}}$), and densities. The latter were found in agreement with experimental values and two models, shown in Figure S3, yield realistic extrapolations of the MD fictive temperatures for laboratory cooling rates, thus validating the potential and MD strategy used. A representative visual illustration of the simulation box was rendered using OVITO basic (Open Visualization Tool) version 3.1.0.[23] To visualize the distribution of Li atoms in the glass, the simulation box was convoluted with a 3D normal distribution function, with σ = 1.0 Å, to obtain the probability density function (PDF) of the distribution. A 2D slice of the obtained PDF was plotted using GNU plot 5.4.

Table 1: Parameters of the potentials used for the MD simulations.[19]

Pair	D_{ij} (eV)	a_{ij} (Å^{-2})	r_0 (Å)	C_{ij} (eV Å^{12})
$Li^{0.6}$—$O^{-1.2}$	0.001114	3.429506	2.681360	1.0
$Si^{2.4}$—$O^{-1.2}$	0.340554	2.006700	2.100000	1.0
$O^{-1.2}$—$O^{-1.2}$	0.042395	1.379316	3.618701	22.0

2.3 Solid-State NMR studies

Solid-State NMR experiments were carried out at 5.64 and 14.10 T on an Agilent DD2 spectrometer (^{1}H Larmor frequency at 243 MHz), and a Bruker Avance 600 Neo spectrometer respectively. The experimental details of all conducted NMR experiments are summarized in Table 2.

Table 2: Larmor frequency υ_0, NMR experiment, nutation frequency ω_{rf}, pulse duration τ_p, MAS frequency υ_{MAS}, recycle delay d_1, number of transients *nt* used in the experiments within this study.

Nucleus	υ_0 / MHz	Experiment	$\omega_{rf}/2\pi$ / kHz	t_p / μs	$\omega_{rf}t_p$	υ_{MAS} / kHz	d_1 / s	*nt*	Reference (shift)	Temperature / °C
^{29}Si	48.15	MAS d.p. [a]	36	7	$\pi/2$	5	600 – 1200	256	TMS (0 ppm)	R.T.
^{7}Li	94.20	Static d.p. [a]	50	0.5	$\pi/8$	static	15	64	1 M LiCl (0 ppm)	-100
^{7}Li	94.20	SATRAS[b]	50	0.5	$\pi/8$	5	2 - 30	65536	1 M LiCl (0 ppm)	R.T.
^{7}Li	94.20	SED[c]	3.1	19, 40.5	$\pi/2$, π	static	10-15	16	1 M LiCl (0 ppm)	-100

[a] d.p. = direct polarization. [b] SATRAS = Satellite Transition Spectroscopy. [c] SED = spin (Hahn) echo decay. [d] SATREC = saturation recovery.

^{29}Si MAS NMR experiments were recorded at a Larmor frequency of 48.15 MHz using a commercial 7.5 mm triple resonance probe operating at υ_{MAS} = 5 kHz. Under the conditions shown in Table 2, 256 transients of 4096 data points were recorded at a dwell time of 10 μs using recycle delays of 600 – 1200 s. ^{7}Li static and MAS NMR experiments were performed at a Larmor frequency of 94.20 MHz in a commercial 4 mm triple resonance probe operating at υ_{MAS} = 5 kHz for the observation of the spinning sideband patterns arising from the non-central ^{7}Li Zeeman transition (satellite transition spectroscopy, SATRAS [24]). All static measurements were conducted at -100 °C to eliminate the effects of motional narrowing on the NMR spectra and 2048 data points were recorded at a dwell time of 10 μs using a recycle delay of 15 s. ^{7}Li static and MAS NMR spectra were simulated assuming first-order quadrupolar lineshapes and distributions of nuclear electric quadrupolar coupling constants (C_Q) according to the Czjzek model [25], implemented in the ssNake software [26]. The latter assumes a normal distribution of the electric field gradient (EFG) tensor components and the resulting probability density function can be expressed in terms of C_Q and η_Q as

$$f(C_Q, \eta_Q) = \frac{C_Q^{d-1}\eta_Q}{\sqrt{2\pi}\sigma^d}\left(1-\frac{\eta_Q^2}{9}\right)\exp\left\{\frac{C_Q^2}{2\sigma^2}\left(1+\frac{\eta_Q^2}{3}\right)\right\}, \quad (3)$$

where η_Q is the asymmetry parameter of the EFG tensor, d is the number of independent tensor components (typically 5, as in the present work), and σ is the standard deviation of the multidimensional Gaussian distribution. Simulations of the spectra of the spin-3/2 ^{7}Li nuclei in the presence of both, electric quadrupolar and magnetic dipole-dipole interactions were performed using the SIMPSON package [27].

SATRAS difference spectra were produced by subtraction of a reference SATRAS spectrum (in this work the as-quenched LS2 glass) from the sample SATRAS spectrum after normalizing both spectra such that their baselines exactly match, leaving just the spectral components not already accounted for in the reference spectrum. For obtaining reliable results it is necessary to record both SATRAS NMR spectra as two consecutive experiments under identical conditions, as every change in MAS spinning rate, transmitter offset frequency, nutation frequency, etc. may produce artificial residual spectra.

To determine the ^{7}Li–^{7}Li dipole-dipole interaction strengths, static ^{7}Li spin-echo decay (SED) NMR experiments were conducted at -100 °C (to remove contributions from dynamic relaxation to the echo decay) using the Hahn spin-echo sequence ($t_{\pi/2} - \tau_1 - t_\pi - \tau_1$). In order to reduce rf-inhomogeneities, only the center third of the used 4.0 mm rotors were filled with sample. A nutation frequency of 4 kHz, as measured on a 0.1 M solution of LiCl, proved sufficiently low to provide the

required selective CT excitation in agreement with prior numerical simulations using the SIMPSON software package. [28, 29] Decay curves were recorded under conditions shown in Table 2, and modeled as Gaussians, which proved valid for multi-spin systems of spin ½ nuclei [30] and valid for pairs of quadrupolar nuclei within the temporal regime of $0 < (2\tau_1)^2 \leq 0.01$ ms² [31] according to

$$\ln\left(\frac{I(2\tau_1)}{I(0)}\right) = -\frac{M_{2\mathrm{E(Li-Li)}}}{2}(2\tau_1)^2. \qquad (4)$$

For $Li_2Si_2O_5$ and the output of the MD simulations second-moment values were calculated via the van-Vleck equation [32]

$$M_2 = f\left(\frac{\mu_0}{4\pi}\right)^2 \gamma_{^7Li}^4 \hbar^2 \sum_{i\neq j} \frac{1}{r_{ij}^6} \qquad (5)$$

where the numerical prefactor f is 9/4 for ^{7}Li with I = 3/2 in the absence of quadrupolar coupling and 0.9562 in the presence of quadrupolar coupling and selective excitation of the central transition. The value f = 9/4 corresponds to the traditional van-Vleck formula for homonuclear dipole-dipole interactions between spin-3/2 nuclei [32]. It is relevant for non-selective excitation of all transitions in cases where the static lineshape of the central transition is dominated by the magnetic dipole-dipole interaction and the quadrupolar satellites are well separated from the central transition. In the present case, this situation applies to the static lineshapes of both crystalline and glassy LS2 samples. The value f = 0.9562 is relevant for the analysis of spin-echo decay spectra, in which the central transition is excited selectively [29]. As discussed below, in the present contribution, this condition was created by low-power excitation and verified by nutation spectroscopy. The second moment measured under these conditions will be denoted $M_{2\mathrm{E(Li\text{-}Li)}}$ in the following.

3. Results, Data Analysis and Discussion

3.1 Differential Scanning Calorimetry

Figure 2 shows DSC curves close to the glass transition event exemplary for as-quenched LS2 glass, and after heat treatments of 1 h, 15 h, 25 d, 40 d, and 60 d (for the DSC curves of all samples see also Figure S4 in the Supporting Information section).

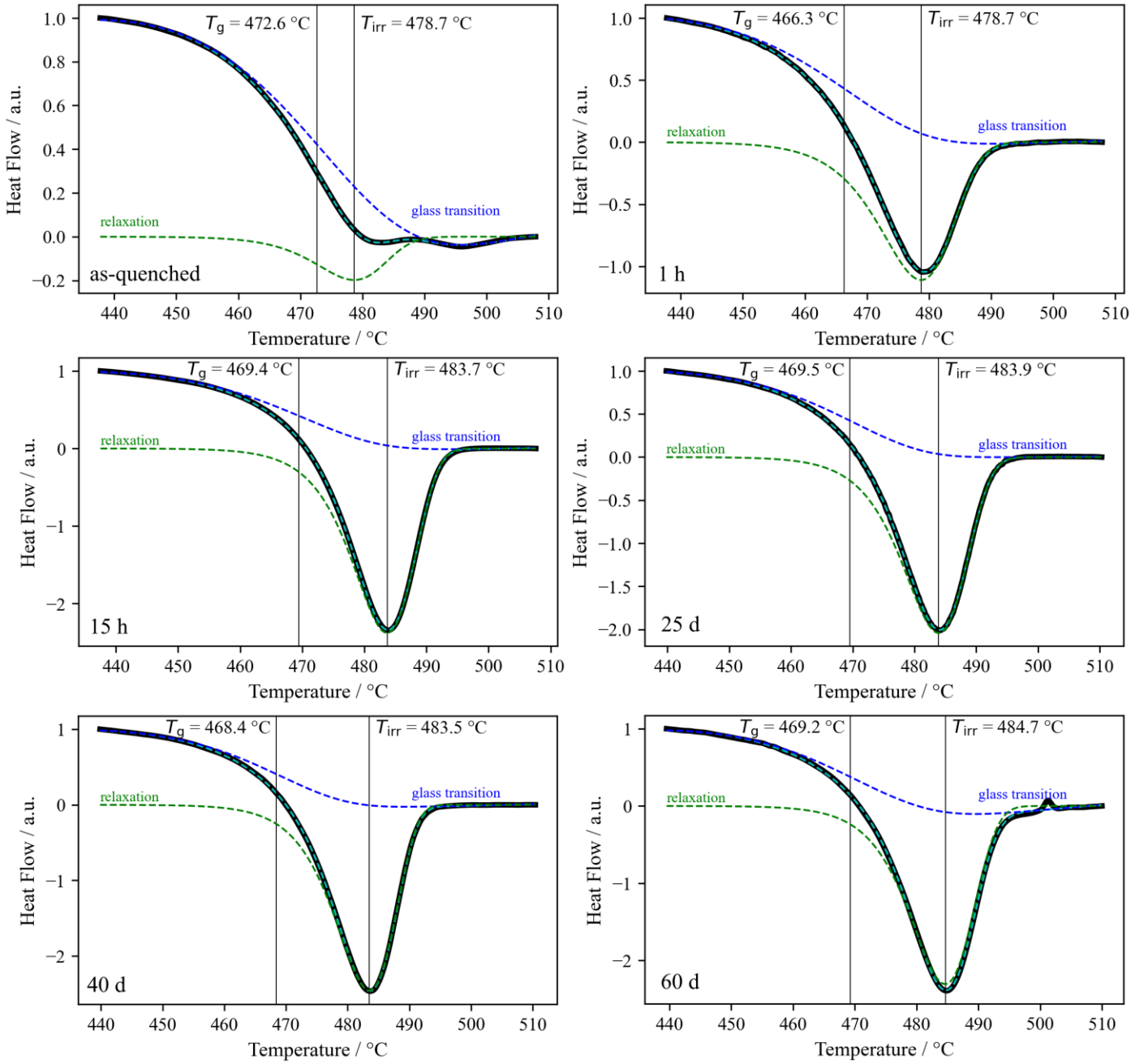

Figure 2: Exemplary DSC curves close to the glass transition event for as-quenched LS2 glass, and after heat treatment at 435 °C for 1 h, 15 h, 25 d, 40 d and 60 d. The cyan dashed line is a fit to the data using an empirical model function consisting of a glass transition part (blue dashed line) and a non-reversing heat flow component (green dashed line), associated with structural relaxation (cf. text for further information).

While for the as-quenched LS2 sample (which had the highest T_f) the glass transition is observed as a characteristic step-wise heat capacity change, the heat-treated glasses (with progressively lower T_f) additionally exhibit an overlapping endothermic event, reflecting the return of the partially relaxed glasses with lower fictive temperatures to a state of higher enthalpy. During the course of the DSC heat treatment, the dynamics when the temperature approaches T_f become sufficiently fast to undo the relaxation process effected by the prior annealing. The magnitude of the latter event increases

with increasing (previous) heat treatment time up to 15 h and significantly affects the tangent of the apparent glass transition inflection point, thus masking the glass transition onset temperature. To overcome this issue, the data were fitted using a mathematical model describing the total heat flow close to the glass transition accounting for this superposition of reversing and non-reversing heat flow processes [33]. From the model, the inflection points of the glass transition event $T_{g,in}$ and the peak of the irreversible contribution T_{irr} were obtained and are listed in Table 3.

Table 3: Apparent onset temperature of glass transition, $T_{g,on}$, modeled inflection point of the glass transition, $T_{g,in}$, modeled peak temperature of non-reversing heat flow, T_{irr}, and peak area of the non-reversing heat flow obtained by the fitting procedure described in the text of Section 3.1.

Sample	$T_{g,on}$ / °C (±0.5 °C)	$T_{g,in}$ / °C (±0.5 °C)	T_{irr} / °C (±0.5 °C)	($T_{g,in} - T_{g,on}$) / °C (±1 °C)	($T_{irr} - T_{g,in}$) / °C (±1 °C)	Non rev. peak area ΔH / J/g (±0.01 J/g)
as-quenched	455.9	472.6	478.7	16.7	6.1	0.02
15 min	454.7	467.9	478.2	13.2	10.3	0.58
30 min	454.6	466.8	478.9	12.1	12.1	0.65
1 h	457.9	466.3	478.7	8.4	12.4	1.06
3 h	464.4	468.0	481.7	3.4	13.7	1.55
15 h	467.8	469.4	483.7	1.6	14.3	1.91
3 d	467.5	468.8	483.6	1.3	14.8	1.86
5 d	467.3	469.7	484.1	2.4	14.4	1.74
6 d	467.1	469.9	484.1	2.8	14.2	1.79
10 d	465.5	468.4	482.9	2.9	14.5	1.67
20 d	466.2	468.7	483.2	2.5	14.5	1.73
25 d	467.5	469.5	483.9	2.3	14.4	1.69
30 d	467.6	469.7	484.4	1.4	14.7	1.82
40 d	468.0	468.4	483.5	0.4	15.1	1.91
60 d	469.0	469.2	484.7	0.2	15.5	1.88

Using the conventional tangent method, the apparent onset $T_{g,on}$ and inflection point of the glass transition for the as-quenched LS2 glass were found to be 456.5 and 472.5 °C respectively, the latter standing in excellent agreement with the inflection point obtained from the fitting model at 472.6 °C. The obtained data clearly shows the effect of glass relaxation on the thermal properties of the glass specimens and some interesting trends can be observed: Most strikingly, the peak area of the non-reversing heat flow increases rapidly with extended heat treatment and reaches a maximum of 1.91 J/g after 15 h. This period is very similar to that measured in an independent study of LS2 glass relaxation using three other techniques by Lancelotti et al. [34], suggesting the glass has reached the stationary state of the supercooled liquid at this temperature marking the end of the non-reversing heat flow event. In samples annealed for longer times, the peak area is found to be slightly decreased over ten days of annealing until it is recovered after about 40 days.

Similarly, $T_{g,on}$, the difference between $T_{g,in}$ and T_{irr}, and the difference between $T_{g,in}$ and $T_{g,on}$ follow this trend closely (the latter inversely). Regarding the characteristic temperatures, initial heat treatment for 15 min reduces $T_{g,on}$ from 455.9 to 454.7 °C, and $T_{g,in}$ from 472.6 to 467.9 °C until both reach a minimum of 454.6 and 466.8 °C, respectively, after 30 min and 1 h. Longer heating results in a joint increase of $T_{g,on}$, and $T_{g,in}$ until reaching a maximum after 15 h of thermal treatment. The results show that structural relaxation is approximately 80% complete after 3 h of thermal treatment at 435 °C, well reproducing the measured values of a recent study tracking LS2 glass relaxation via thermal analysis, ionic conductivity, and refractive index[34].

Interestingly, however, while $T_{g,on}$ and T_{irr} continually increase with thermal treatment time, $T_{g,in}$ and the peak area of the enthalpic relaxation stay rather constant for annealing times > 15h. This implies a symmetry change of the logistic function derivative (used in modeling the non-reversing thermal event) under conservation of the total area after 15 h of heat treatment, which may be possibly connected to the onset of nucleation. To test this hypothesis and evidence any structural changes during the heat treatment, in the following, the landmark samples, namely as-quenched glass, and glasses annealed for 15 min, 1 h, 15 h, 10 d, 25d, 40 d, and 60 d were further spectroscopically investigated.

3.2 X-Ray powder diffraction

Figure S1 shows results from X-ray diffractometry. The absence of sharp diffraction peaks in the original quenched glass and in all samples treated up to 15 d of thermal treatment (data not shown) confirm the fully amorphous character of the samples studied. Small amounts of Li_2SiO_3 (LS) are detected after annealing times of 25 d, and the formation of crystalline LS2 becomes clearly evident in the samples heated for 40 d and 60 d. As discussed below, the level of crystalline LS in any of these samples is below the detection limit of ^{29}Si MAS-NMR.

3.3 Raman Spectroscopy

Raman spectroscopy was performed to evidence potential structural changes in the short- to intermediate-range order of the LS2 glass network with sub-T_g heat treatment. Figure 3 shows the Raman spectra for the samples under study.

Vibrational bands, characteristic of the asymmetric Si–O modes in LS2 glass can be observed near 470 (Q^4), 580 (Q^3), 665 (Q^2), 780 (assignment uncertain), 950 (Q^2), 1030 (Q^4), 1080 (Q^3), and 1120 (Q^3/Q^4 superposition) cm^{-1} [9, 35]. Despite some minor changes in the baseline above 1200 cm^{-1}, no significant changes in the Raman bands can be observed with increasing sub-T_g heat treatment

up to 15 h, suggesting no appreciable changes in the short- and intermediate-range order of the silicate network.

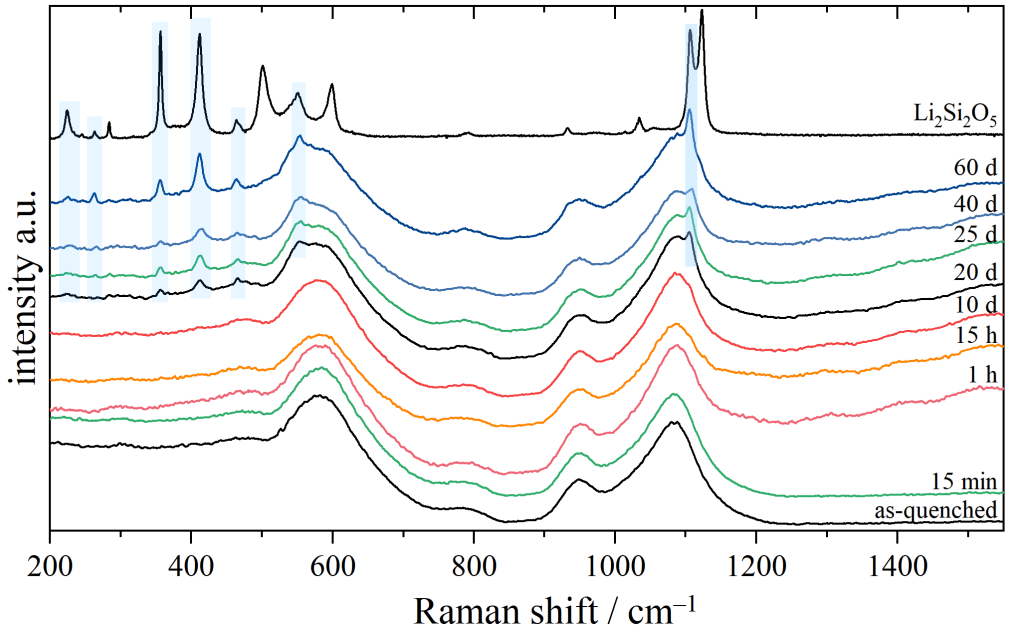

Figure 3: Raman spectra of $Li_2Si_2O_5$, as-quenched LS2 glass, and LS2 glass after heat treatment at 435 °C for the times indicated in the figure. Sharp peaks at 225, 262, 356, 412, 464, 551, and 1106 cm^{-1} have been indicated, suggesting the presence of nucleated LS2.

Recently, Jurca et al. [36] reported the results from sub-T_g heat treatment of a commercial Na-Ca-Mg-silicate float glass and discussed the observed changes in the deconvolutions of the Raman spectra in the context of structural relaxation, indicating a shift in the $Q^2 + Q^4 \leftrightarrow 2Q^3$ (dis)synproportionation reaction towards the formation of more Q^3 units. For the samples of the present study, however, such shifts in the bands were not observed. Given that Raman spectroscopy is an inherently non-quantitative method and the correction of the baseline can be a rather ambiguous process, we refrained from further spectral analyses in the present case. The Raman spectra do show, however, weak sharp features at 225, 262, 356, 412, 464, 551, and 1106 cm^{-1} in all samples heated beyond 15 h, which progressively increase, suggesting the presence of nucleated LS2 [37]. Their Raman profile differs from the one of bulk $Li_2Si_2O_5$, possibly indicating that the crystal nuclei initially formed are a polymorph of the well-known equilibrium phase. Metastable LS2 polymorphs have been previously observed [12, 13] and were elsewhere implicated in the nucleation process of lithium disilicate glass [15]. On the other hand, our data give no evidence of lithium metasilicate nucleation, which has been reported in other studies, of stoichiometric [15] and off-stoichiometric [13] LS2

glasses. The Li_2SiO_3 (LS) phase would give rise to strong scattering peaks at 983 cm^{-1} (B_2 mode) and 610 cm^{-1} (A_1 mode) [38] which are not observed in the samples of the present study.

^{29}Si MAS NMR with long relaxation delays (20 min) discussed further below, shows that the crystalline fraction of $Li_2Si_2O_5$ in this sample is close to 1% in a sample treated at 435 °C for 40 d. This fraction increases to 3% after 60 d annealing.

3.4 ^{29}Si NMR

To probe the short-range ordering of the silicon network makeup, ^{29}Si MAS NMR spectra were recorded on the samples under study and the results are shown in Figure 4.

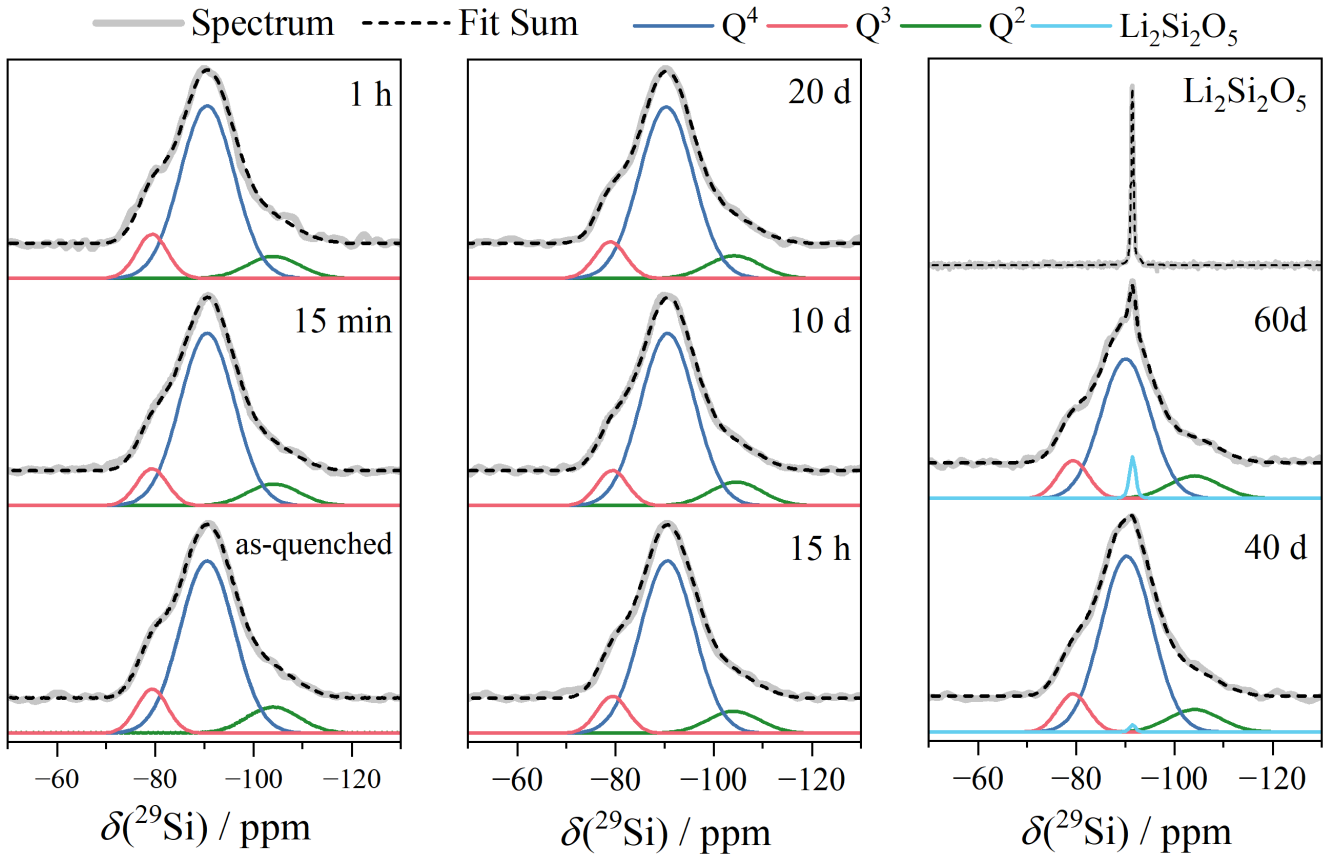

Figure 4: ^{29}Si MAS NMR spectra of as-quenched LS2 glass before and after heat treatment at 435 °C for the depicted duration. Blue, red, and green lines are fit components of the spectral deconvolution attributable to Q^4, Q^3, and Q^2 units respectively.

The spectra were deconvoluted into three Gaussian lineshape components, corresponding to Q^4, Q^3, and Q^2, units, standing in good agreement with deconvolutions of prior works. [7, 39] The extracted NMR parameters are listed in Table 4. While a glass with a stoichiometric composition of $Li_2O{\cdot}2SiO_2$ could be made up entirely of Q^3 units like its isochemical crystal, the above-mentioned disproportionation (1) leads to multiple Q^n units. In the present case, equal amounts of 11±1% Q^4 and

Q^2 units are observed for as-quenched LS2 glass corresponding to an equilibrium constant of K_3 = 0.0198.

Heat treatment of 15 min appears to slightly reverse the disproportionation, however, the observed changes are within the error limits. Interestingly, the area fractions of the latter two units behave rather invariantly under thermal treatment within the error of the experiment until, after 40 d, the formation of a narrow Q^{3C} signal, attributable to crystalline $Li_2Si_2O_5$, can be observed near -92 ppm. In the course of the advancing crystallization, the Q^{3C} area fraction increases at the expense of principally the Q^3 units in the glass, also slightly decreasing the linewidth of the latter signal. The crystalline $Li_2Si_2O_5$ exhibits a rather narrow resonance that was deconvoluted into a dominant component with an isotropic chemical shift of -91.5 ppm and a minor low-frequency component at a somewhat lower shift of -92.8 ppm (see Figure S5 Supporting Information).[9] The latter signal may reflect a different LS2 polymorph or a defect site.[13] In agreement with the Raman results, the NMR spectra also do not evidence any LS formation (no sharp signal near -75 ppm [13]). Its area fraction may be underestimated owing the relaxation delay used (20 min) in these experiments, which may be less than five times the spin-lattice relaxation time of this component (which could not be precisely determined).

Table 4: ^{29}Si isotropic chemical shifts, full width at half maximum, and area fractions extracted from MAS NMR lineshape simulations. Values in parenthesis describe the individual contributions ($FWHM_{Lorentzian}$ + $FWHM_{Gaussian}$) to the overall FWHM of a mixed Gaussian-Lorentzian line. Q^{3c} represents the signal of $Li_2Si_2O_5$ visible in the glasses while Q^{3a} and Q^{3b} correspond to two Q^3 species in the MAS NMR spectrum of $Li_2Si_2O_5$.

Sample	δ_{iso} / ppm (± 0.2 ppm)				FWHM / ppm (± 0.2 ppm)				Area fraction / % (± 1%)			
	Q^4	Q^{3c}	Q^3	Q^2	Q^4	Q^{3c}	Q^3	Q^2	Q^4	Q^{3c}	Q^3	Q^2
As quenched	-104.1	-	-90.6	-79.4	12.5	-	13.0	7.4	11	-	78	11
15 min	-104.1	-	-90.6	-79.4	12.5	-	13.0	7.4	10	-	80	10
1 h	-104.1	-	-90.6	-79.4	12.5	-	13.0	7.4	10	-	79	11
15 h	-104.1	-	-90.6	-79.4	12.5	-	13.0	7.4	10	-	80	10
40 d	-104.1	-91.5	-90.3	-79.4	12.5	(0.5 + 1.2)	12.4	7.4	10	1	79	10
60 d	-104.1	-91.5	-90.1	-79.4	12.5	(0.5 + 1.2)	12.0	7.4	12	3	73	12
		Q^{3a}	Q^{3b}			Q^{3a}	Q^{3b}			Q^{3a}	Q^{3b}	
$Li_2Si_2O_5$	-	-91.5	-92.8	-	-	(0.3 + 0.4)	1.0	-	-	92	6	-

3.5 MD Simulations

In agreement with a previous study [40], while overall consistent with the charge balance demands at the LS2 composition, our MD simulations show no influence of the quenching rate and the resulting T_f on the Q^n distribution of the network former units (NFUs), in this high-temperature range, which

is above the SCL state, see Table 5. In this case, the MD-generated NFU distributions correspond to a complete randomization (binomial distribution) of the Q^n inventory. In contrast, the ^{29}Si NMR spectra of the glasses (with 78% Q^3 units) represent structures with significantly lower T_f (450-500 °C). Nevertheless, Figure S3 shows that an extrapolation of the quench-rate dependent T_f values obtained in the simulations, using the MYEGA [41] model of viscosity approach the experimental T_g values, confirming the validity of our MD results. Reference [40] had also demonstrated that structural changes between LS2 glasses with different fictive temperatures are observed principally in terms of lithium local structure. Thus, lower cooling rates, corresponding to glasses with lower fictive temperatures, may result in the clustering of Li-ions or a systematic change in their clustering. To experimentally verify this simulative result, we have first reproduced MD simulations for the LS2 composition with various quench rates (see also SI for the resulting radial distribution functions). An example of a 2D slice of simulation box showing the Li atomic densities is presented in Figure 5a. For a randomly selected lithium-ion *i* the outputs of the structure from the MD simulations were used to calculate the sum of the inverse sixth power distances (distance sum) to all neighboring Li atoms *j*, $\sum_{i \neq j} \frac{1}{r_{ij}^6}$, which relates to the ^{7}Li–^{7}Li homonuclear dipole-dipole second moments $M_{2(\text{Li-Li})}$ via Eq. (5).

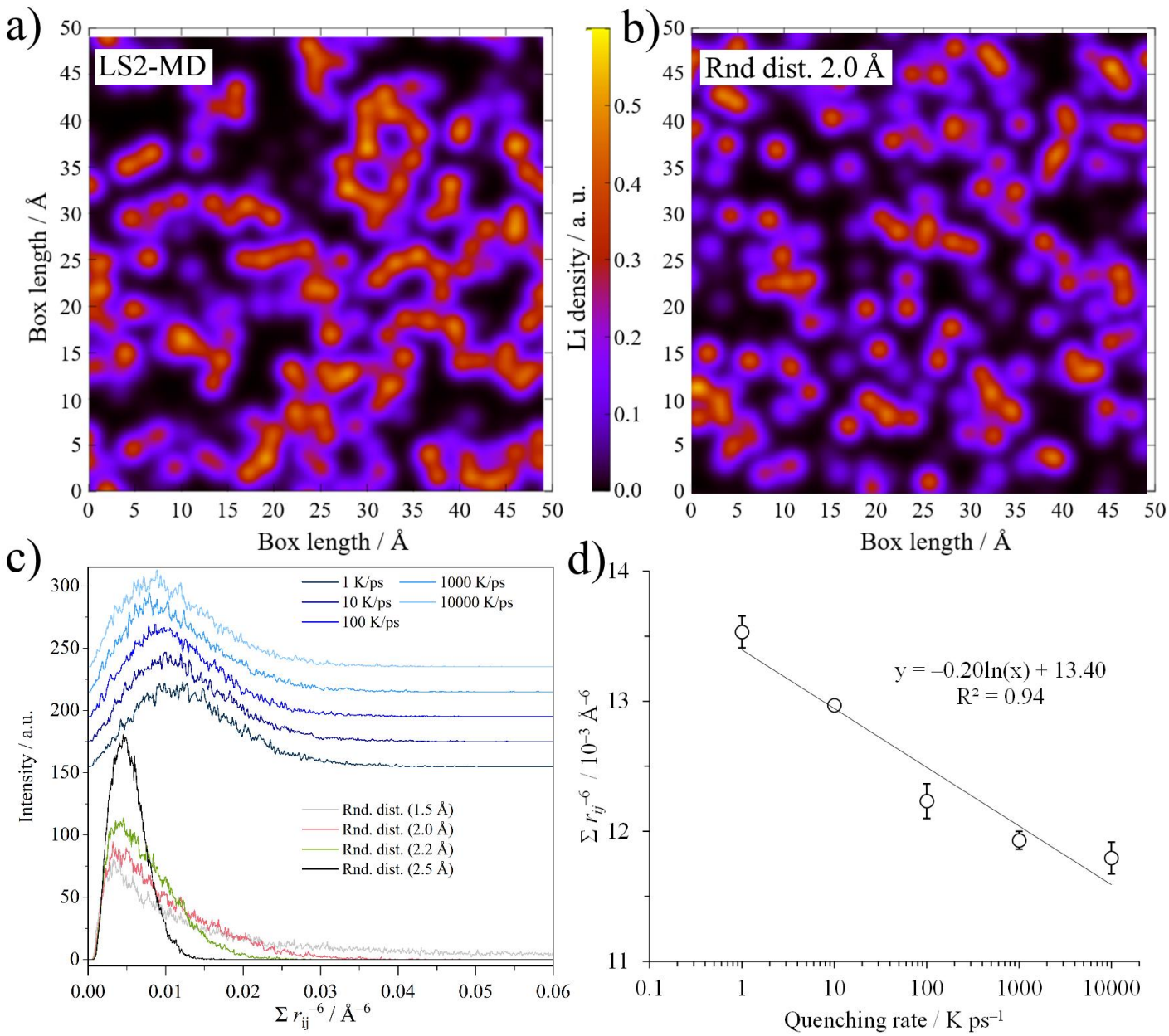

Figure 5: (a) Simulated spatial lithium density distribution scenarios: (a) Cross-section of the simulation box for the MD simulation of glassy lithium disilicate: (b): Cross-section of the simulation box for a truncated random distribution assuming the same number density as in the LS2 simulation (c): Distribution of distance sums Σr^{-6} for different quench rates in the LS2 simulation box (top) and in the truncated random distribution box (bottom) based on different cutoff values for the closest possible distances (in parenthesis). (d): Quench rate dependence of distance sums Σr^{-6} for MD-simulated LS2 glass. The vertical bars correspond to the data's standard deviation obtained from three distinct simulations.

During this procedure, only 92.58% of the Li atoms were considered, accounting for the natural abundance of the ^{7}Li isotope, and the resulting distance sums were binned into a histogram. The above procedure was repeated 1,000 times and an average distance sum was extracted after normalization of the histogram through integration. Figure 5 c) shows the distribution of $\sum_{i \neq j} \frac{1}{r_{ij}^{6}}$ values obtained for the randomly chosen ^{7}Li nuclei, and Figure 5 d) presents the distribution's average as a function of

quenching rates. The results show a clear trend, indicating a significant increase of $\sum_{i \neq j} \frac{1}{r_{ij}^6}$ and thus $M_{2(\text{Li-Li})}$ values for decreasing fictive temperatures. We note that these M_2 values appear to be by about a factor 2 higher than those calculated from an MD study published previously [42]. While the origin of this discrepancy is not clear we note that our values (see Table 5) are close to the experimental ones measured by NMR (Table 6, see below).

Table 5: Distance sums Σr^{-6} for the MD simulations for different cooling rates calculated from the center of gravity (*CG*) of the Σr^{-6} distribution and the resulting predicted $M_{2E(\text{Li–Li})}$ values assuming a prefactor $f = 0.9562$ ($M_{2(\text{Li–Li})}$ values using $f = 9/4$ in parenthesis) for Eq. 2. Errors correspond to the standard deviation obtained from averaging three simulations.The bottom part shows the calculated result for a truncated random distribution with different cut-off distances.

Cooling rate / K/ps	T_f / °C (± 0.5 °C)	$CG(\Sigma r^{-6})$ / 10^{-3} Å^{-6} (± 0.1^{-3} Å^{-6})	$M_{2(\text{Li-Li})}$ / 10^6 rad²/s² (± 2.5×10^6 rad²/s²)	Q^n distribution / % (± 0.2 %)				
				Q^4	Q^3	Q^2	Q^1	Q^0
1	770.0	13.5	155 (465)	29.8	45.2	20.9	3.9	0.2
10	920.0	12.9	148 (349)	29.9	44.8	21.6	3.4	0.3
100	1102.0	12.2	140 (329)	29.8	44.9	21.7	3.4	0.2
1000	1780.0	11.8	136 (319)	30.1	44.8	21.4	3.6	0.2
10000	-	11.7	134 (316)	29.4	45.9	20.8	3.6	0.2
Rnd. dist								
1.5 Å		11.2	129 (303)					
2.0 Å		9.8	113 (265)					
2.2 Å		7.5	86 (203)					
2.5 Å		5.4	62 (146)					

Figure 5 also presents an alternative scenario based on a random lithium-ion distribution having the same ion density as LS2 glass (Figure 5b)). These random distributions were simulated assuming different "cut-off"- distances, limiting the shortest possible Li–Li distance in the structure. As expected, this scenario yields M_2 distributions with significantly lower average values, if realistic cut-off distances (2.2 or 2.5 Å) are assumed. Thus, the MD result suggests that the lithium distribution in glassy LS2 shows a significant degree of clustering and cannot be described by a random distribution model. Indeed, first evidence of this result was reported by an early isotope-selective neutron diffraction study on LS2 glass [43], which is further confirmed in the present study by the NMR results discussed below.

3.6 ^{7}Li dipolar NMR

Figure 6 shows static ^{7}Li NMR spectra, recorded at -100 °C to remove motional narrowing effects on the lineshapes. Only the spectral region of the central Zeeman transition is shown. For all the glasses,

wide signals are observed, which could be simulated by a mixed Gaussian/Lorentzian lineshape function. In contrast, crystalline $Li_2Si_2O_5$ exhibits a broadened two-peaked lineshape suggesting a dominant two-spin interaction. Indeed, this lineshape was also observed in previous studies [5, 14], which have pointed out it to be unexpected in view of the crystal structure of LS2, as the shortest Li—Li distance of 2.45 Å [44, 45] is not significantly different from the four additional Li–Li next nearest neighbor distances encountered in both, the thermodynamically stable and the metastable form of crystalline LS2 [44-46]. The dipolar vectors in both forms of crystalline LS2 are, however, arranged in a highly anisotropic fashion, such that no Gaussian lineshape would be expected as a powder average of the dipolar interactions in this multi spin system. A rigorous lineshape simulation including all the relevant dipolar and quadrupolar interactions encountered in this LS2 multispin system is beyond the limit of standard computational resources. In the present contribution, we use a simplified procedure, treating the multi-spin interaction in terms of a two-spin interaction with an effective dipolar coupling constant comprising the total interaction strength (second moment) of the multi-spin network. As shown in Figure 7, this approach leads to an excellent agreement with the experimental lineshape, based on a quadrupolar coupling constant of C_Q = 84 kHz (in agreement with the total span of the satellite transition (SATRAS) spectra, discussed below), a relative inclination of both EFG tensor's principal axes by β = 30°, and an effective dipolar coupling constant $|d|$ of 1.97 kHz. The corresponding second moment calculated from this d-value, $M_{2(\mathrm{Li\text{-}Li})} = 9/4\times(2\pi|d|)^2 = 343.7\times10^6$ rad²/s², is in acceptable agreement with the value of 319.46×10^6 rad²/s² predicted by the van Vleck equation for the homonuclear interactions (pre-factor 9/4).

Figure 6 shows further that the ^{7}Li static NMR lineshapes are close to Gaussians, revealing that the lithium ions in the glassy state are clearly differently arranged than in crystalline LS2. In the present system, we can assume the line shapes are dominated by the homonuclear ^{7}Li-^{7}Li dipolar couplings, as the heteronuclear dipole couplings to ^{29}Si and ^{6}Li can be neglected because of the low natural abundances of these isotopes. Furthermore, there seem to be no indications of the satellite transitions overlapping with (or producing shoulders near) the Gaussians representing the central transitions.

The second moment of a Gaussian resonance and the full width at half maximum, *FWHM* are related according to [47]

$$FWHM = 2\sqrt{2\ln 2\, M_{2(\mathrm{Li-Li})}} \qquad (6)$$

leading to the $M_{2(Li-Li)}$ values listed in Table 6 for the samples under study. For as-quenched LS2 glass, an $M_{2(Li-Li)}$ value of 365.2×10^6 rad²/s² is found, which is of comparable size to the second-moment values obtained from the MD simulations considering Eq. (5). Also, in the heat-treated samples, the $M_{2(Li-Li)}$ values tend to increase with increasing annealing time, reflecting the effect of decreasing fictive temperature. Again, this result stands in excellent agreement with the trends shown by the MD simulations. We note, however, that the NMR spectra are not purely Gaussian, and the Gaussian/Lorentzian ratio increases, principally for samples annealed for 40 and 60 d, resulting in some uncertainty of the experimental second-moment values deduced from the static lineshapes via eq, (6).

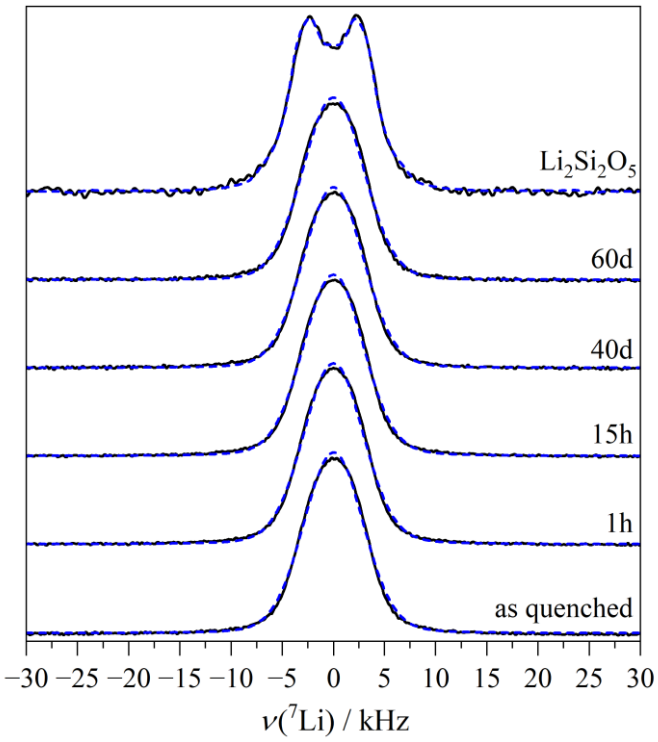

Figure 6: Static ^{7}Li NMR spectra recorded at -100 °C. Blue curves indicate simulations as discussed in the text.

Table 6: ^{7}Li center of gravity δ_{CG}, full width at half maximum of the resonance lines, *FWHM*, thereof derived ^{7}Li-^{7}Li dipole-dipole second moments, $M_{2(Li-Li)}$ deduced from the lineshape via eq. (6), Gauss/Lorentz ratio of fits to the data, and $M_{2E(Li-Li)}$ values from spin-echo decay experiments via eq. (4).

Sample	δ_{CG} (MAS) / ppm (± 0.2 ppm)	*FWHM* (MAS) / kHz (± 0.02 kHz)	*FWHM* (static) / kHz (± 0.02 kHz)	$M_{2(Li-Li)}$ / 10^6 rad²/s² (FWHM) (± 2.5×10^6 rad²/s²)	Gauss/Lorentz ratio (Gaussian percentage)	M_{2E} / 10^6 rad²/s² (SED) (± 2.5×10^6 rad²/s²)
As-quenched	-0.2	0.53	7.16	365	7.70 (88.5%)	99
15 min	-0.2	0.54	7.12cd	362	7.80 (88.8%)	101
1 h	-0.2	0.54	7.19	368	7.96 (88.8%)	122

15 h	-0.2	0.53	7.23	372	7.31 (88.0%)	124
40 d	-0.2	0.55	7.22	371	9.64 (90.1%)	122
60 d	-0.2	0.55	7.35	385	13.95 (93.3%)	112
$Li_2Si_2O_5$	0.0	1.19	-	344 (2 spin simulation, c.f. text)	(d = -1967 Hz)	131

As an alternative approach to the lineshape analysis discussed above, dipolar coupling information related to homonuclear ^{7}Li second-moment values can also be obtained by ^{7}Li spin-echo decay experiments. This method was first proposed by Haase and Oldfield for quadrupolar nuclei [29], subsequently applied to ^{23}Na ion distributions in glasses [31], and recently also applied for the first time to ^{7}Li in lithium silicate glasses [11]. It has the advantage that heteronuclear dipole-dipole interactions as well as chemical shift anisotropies and distributions, which might affect the static lineshape are eliminated. To avoid interference of quadrupolar interactions the experimental conditions must be chosen such, that only the central transition is selectively excited. These experiments use excitation at rather low power, with selective 90° and 180° pulse lengths near 20 μs and 40 μs in the present case, corresponding to a non-selective nutation frequency of 6.2 kHz on the sample. The obtention of the selective excitation regime was confirmed by both SIMPSON simulations and systematic nutation experiments.

Figures 7 and S6 show the results for as-quenched LS2 glass, after heat treatment for 15 h and 60 d, and crystalline $Li_2Si_2O_5$.

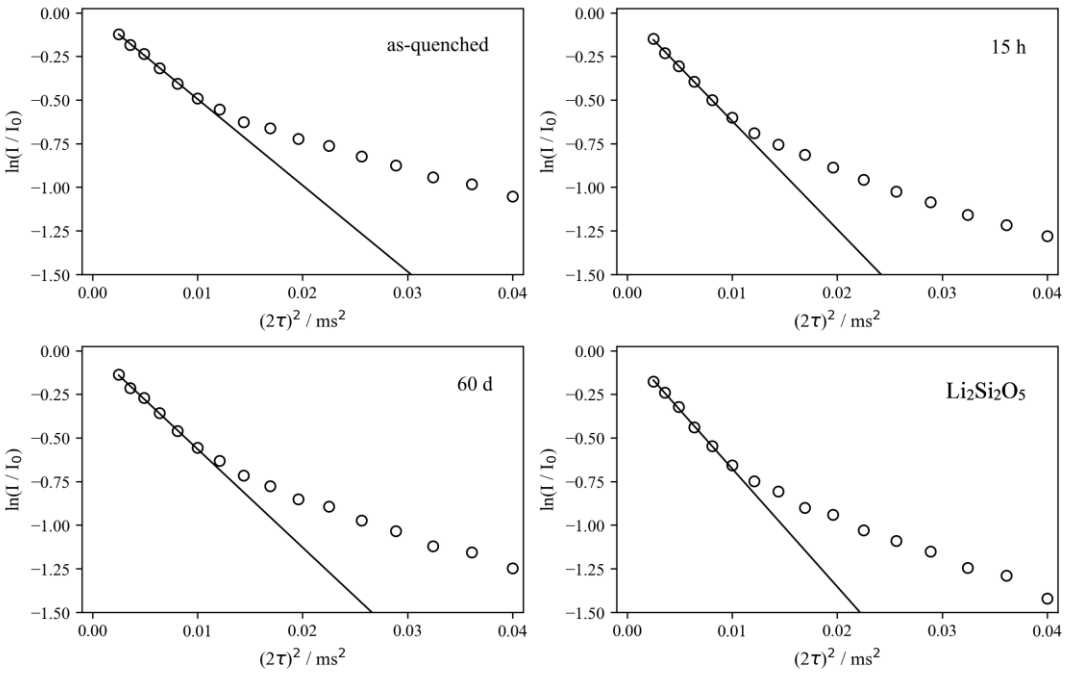

Figure 7: Representative static ^{7}Li spin-echo decay curves, measured at -100 °C. The solid line is the least-squares fit to the data in the regime $0 \leq (2\tau)^2 \leq 0.01$ ms². The experimental error corresponds to the symbol size.

For crystalline $Li_2Si_2O_5$ we measure $M_{2E(Li\text{-}Li)} = 131.1\times10^6$ rad²/s² which stands in excellent agreement with the theoretical value of 137.5×10^6 rad²/s² obtained from eq. (5) based on the reported crystal structure by de Jong et. al. [45]. As in this experiment, only the ^{7}Li nuclei in the central Zeeman states are involved, the second-moment values obtained in this fashion differ numerically from those determined from the lineshape via equation (6), and are herewith denoted $M_{2E(Li\text{-}Li)}$. As previously shown [11, 31] $M_{2E(Li\text{-}Li)}$ relates to structure via eq. (5) using the prefactor 0.9562. In the present study, $M_{2E(Li\text{-}Li)}$ values were obtained to a good approximation by fitting the data to a Gaussian decay in the regime $0 < (2\tau)^2 \leq 0.01$ ms². For longer dipolar mixing times, the spin-echo decay amplitudes are no longer satisfactorily described theoretically by eq. (4), leading to deviations of the experimental data from the predicted behavior.

Consistent with the lineshape analysis presented above, the $M_{2E(Li\text{-}Li)}$ values measured via the spin-echo decay method also tend to increase upon heat treatment, evidencing the decrease of average Li–Li distances as glass relaxation progresses. Furthermore, the overall magnitude of the trend (15-20%) is in excellent agreement with that (13.5%) observed in the quench-rate-dependent MD simulation data. After reaching a maximum value of 122.3×10^6 rad²/s² for the fully relaxed glass (15 h), we observe a small reduction of the $M_{2(Li\text{-}Li)}$ values for longer heat treatments, possibly reflecting some alterations in the residual glass driven by the onset of nucleation.

3.7 ^{7}Li quadrupolar NMR

In principle, any changes in the ^{7}Li local environment due to structural relaxation or crystallization may also affect the magnetic shielding experienced by the ^{7}Li nuclei, as well as the local electric field gradients they are exposed to, leading to changes in chemical shifts and quadrupolar couplings. In practice, however, ^{7}Li chemical shifts are fairly insensitive to changes in Li coordination environments, bond lengths and angles, and vary within a few ppm only. Variations in ^{7}Li nuclear quadrupolar coupling strengths, on the other hand, are significantly larger between different compounds. ^{7}Li quadrupolar interactions manifest themselves quite distinctively in the spread and shape of the satellite transitions (STs), which are commonly observed and quantified from MAS NMR experiments, in which they produce spinning sideband manifolds. In the slow-spinning limit ($\nu_r << \nu_Q$) the spinning sideband intensity pattern forms the envelope of the static powder pattern of the satellite transitions, making it possible to determine the quadrupolar coupling constants C_Q and electric field gradient asymmetry parameters η_Q by simulation (satellite transition, SATRAS spectroscopy).

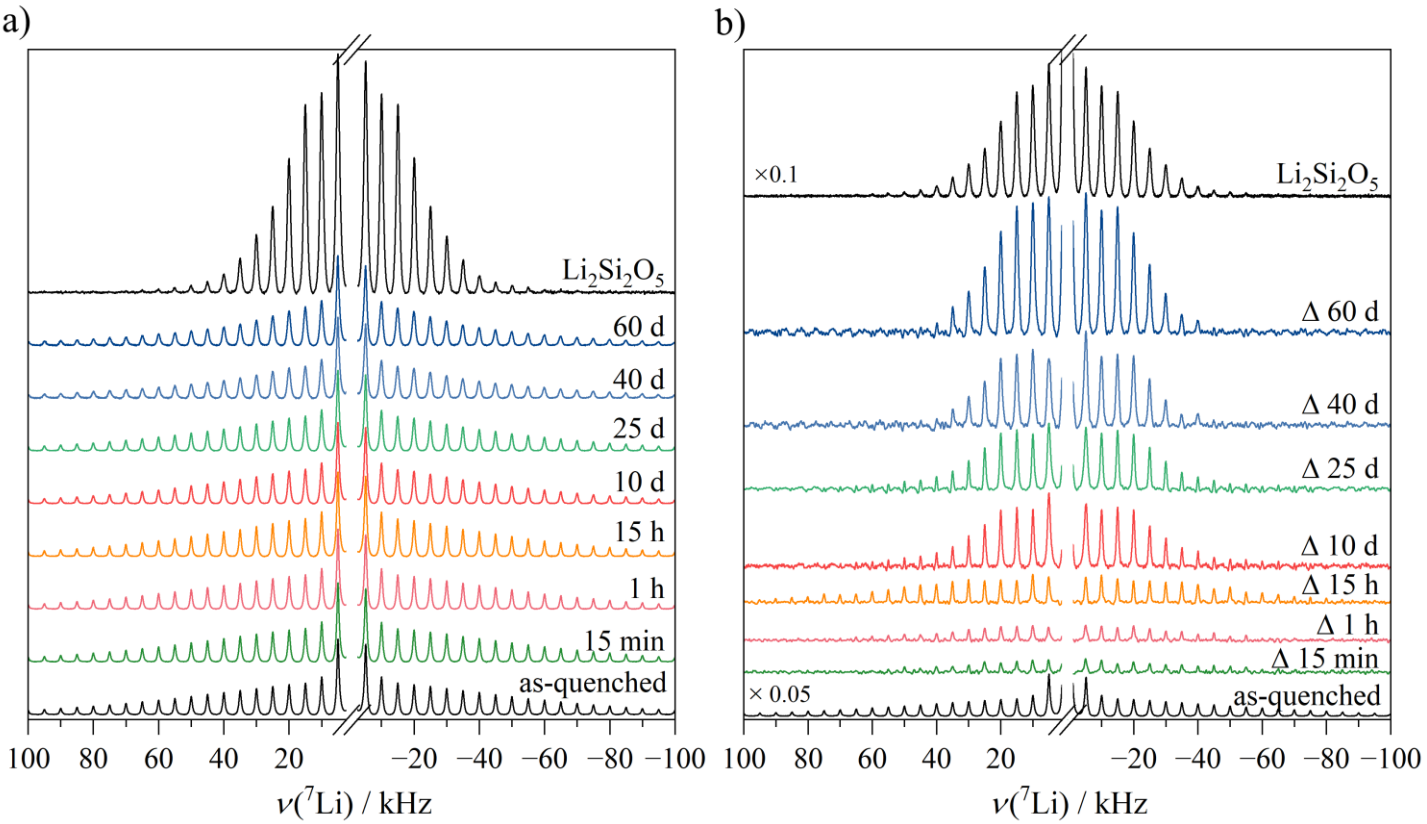

Figure 8: a) ^{7}Li SATRAS NMR spectra recorded at υ_{MAS} = 5 kHz and b) difference spectra calculated via SATRAS(sample) – SATRAS(as-quenched glass). The central peaks have been truncated for increasing the visibility of the spinning sidebands.

Figure 8 (left) shows part of the ^{7}Li SATRAS NMR spectra for selected samples. Invariant isotropic chemical shifts and only minor increases in the central-transition (CT) widths can be observed for all samples (see Figure S7, Supporting Information, and Table 7). Figure 8 shows that the CTs are accompanied by a number of spinning sidebands stemming from the STs while within the resolution, governed by the employed MAS spinning rate of 5 kHz, a total span of 310±2 kHz is observed for all the samples. We note that the spinning rate is insufficient to completely average the strong homonuclear dipolar broadening of the CT, which increases the intensity of the first set of spinning sidebands. While for a glass a distribution of local EFGs around the ^{7}Li spins is expected, the total span of the spinning sideband pattern corresponds to the largest EFGs detectable in the glass within the limitations of the signal-to-noise ratios. In fact, the spinning sideband profile can be sufficiently well simulated assuming a Czjzek distribution of quadrupolar parameters (data not shown) when the CT and the first two sets of spinning sidebands are excluded, however, the distribution widths are rather invariant for the samples under study, see Table 7.

Figure 8 also shows that the spinning sideband patterns observed for the glasses are drastically different from those observed for crystalline LS2 suggesting a significant difference in the quadrupolar interaction strengths and their distribution. Furthermore, as illustrated in Figure 9 (top), the spinning sideband pattern of crystalline LS2 can only be simulated satisfactorily when taking into account the effective two-spin dipole-dipole coupling that is responsible for the static lineshape. Table 7 summarizes all the observables extracted from the sideband patterns.

Table 7: ^{7}Li Center of gravity, δ_{CG}, Full width at half maximum, *FWHM*, peak C_Q values and distribution widths σ of Czjzek distributions, asymmetry parameter of EFG tensor η_Q, and normalized SATRAS difference signal intensity Δ.

Sample	δ_{CG} (MAS) / ppm (± 0.1 ppm)	*FWHM* (MAS) / kHz (± 0.05 kHz)	C_Q / kHz (σ / kHz) (SATRAS) (± 5 kHz)	C_Q / kHz (σ / kHz) (Difference Spectra) (± 5 kHz)	η_Q (± 0.05)	Gaussian Broadening / Hz (Lorentzian broadening CT/ST)	Difference area fraction Δ / % (± 0.2 %)
Glass	-0.2	0.53	163 (93)	-	-	-	-
15 min	-0.2	0.54	163 (92)	112[a] (65)	-	788	1.5
1 h	-0.2	0.54	163 (92)	112[a] (63)	-	769	1.7
15 h	-0.2	0.53	153 (88)	153[a] (85)	-	707	3.7
10 d[b]	-0.2	0.53	153 (87)	93	0.27	487	6.5
25 d[b]	-0.2	0.54	153 (87)	94	0.24	492	6.3
40 d[c]	-0.2	0.55	153 (88)	90	0.24	500	8.2
60 d[c]	-0.2	0.55	153 (87)	90	0.24	500	14.9
Cryst[c]	0.0	1.19	82 (η_Q = 0.18)	-	-	784 (100)	-

[a]peak C_Q values of Czjzek distribution [b] Two-spin simulation with $|d|$ = -1.967 kHz and relative orientation of first spin's EFG principal tensor axis towards the dipolar vector and external magnetic field of β = 30°. [c]Two-spin simulation with $|d|$ = -1.985 kHz and relative orientation of first spin's EFG tensors towards the dipolar vector and external magnetic field of β = 30°.

While at first glance the spinning sideband patterns of the glasses with their different annealing histories look rather similar (Figure 8, left), interesting changes can be revealed by looking at SATRAS difference spectra. To this end, the spectra were normalized such that the outermost spinning sidebands exhibit the same intensity as those of the as-quenched sample and, subsequently, the spectrum of the as-quenched sample was subtracted, see Figure 8 (right). These difference spectra show that the annealed glasses have significant lineshape contributions not present in the base glass: For short heat treatment times, a set of spinning sidebands with a shallow intensity profile similar to the regular SATRAS spectrum of the as-quenched glass can be observed with the total span reaching about 190 kHz after 15 h. This difference spectrum reveals that the electric field gradient distribution at the ^{7}Li nuclei does undergo changes upon structural relaxation, even though the Czjzek simulation parameters of the quenched glass and the 15 h annealed glass are rather similar. Thus, the structural relaxation effect on the electric field gradient distribution appears to be relatively subtle, yet

detectable. Beyond 15 h of annealing time, the spinning sideband profiles of the SATRAS difference spectra become drastically steeper and narrower, in fact, they closely resemble that of the regular SATRAS spectrum of $Li_2Si_2O_5$. For the samples heat-treated for 40 d and 60 d the area fractions of the ^{7}Li SATRAS difference spectra (compared to the regular SATRAS spectrum of each sample) are 8.2 and 14.9 %, respectively, which is significantly higher than the area fractions of crystalline $Li_2Si_2O_5$ detected via ^{29}Si MAS NMR. We attribute this SATRAS difference intensity to the crystalline fraction of $Li_2Si_2O_5$ and point out the much higher precision of this quantification approach compared to ^{29}Si MAS NMR.

For samples annealed for 10 d and 25 d, the difference spectra also look very similar to those of the 40 d and 60 d samples. In addition, a satisfactory simulation of their spinning sideband profile also requires the inclusion of the effective two-spin dipolar Hamiltonian used for the simulation of the pattern in crystalline LS2. These simulations are summarized in Figures 9 and S8 in the Supporting Information section. Thus, while for samples heat-treated for up to 15 d the Czjzek model is sufficient, the simulations of the difference spectra done on the samples obtained at all the longer heat treatments include the dipolar coupling close to the ^{7}Li–^{7}Li effective two spin system ($d \sim -1.97$ kHz), and quadrupolar coupling parameters relatively close to those measured in $Li_2Si_2O_5$. Based on the evidence outlined above we attribute these difference spectra to nascent $Li_2Si_2O_5$ crystal nuclei. We suspect that the 10 d and 25 d samples do not give rise to sharp ^{29}Si MAS-NMR lines (in Figure 4) because the nucleated crystals are too small in size. In very small particles the large fraction of ^{29}Si nuclei at or near the surface would lead to a distribution of ^{29}Si chemical shifts, as the ^{29}Si nuclei at or near the surface find themselves in significantly different bonding environments than those in the interior. On the other hand, the Raman spectra (Figure 3) of the 25 d sample does give evidence of some sharp features that may also be attributable to LS2 nuclei.

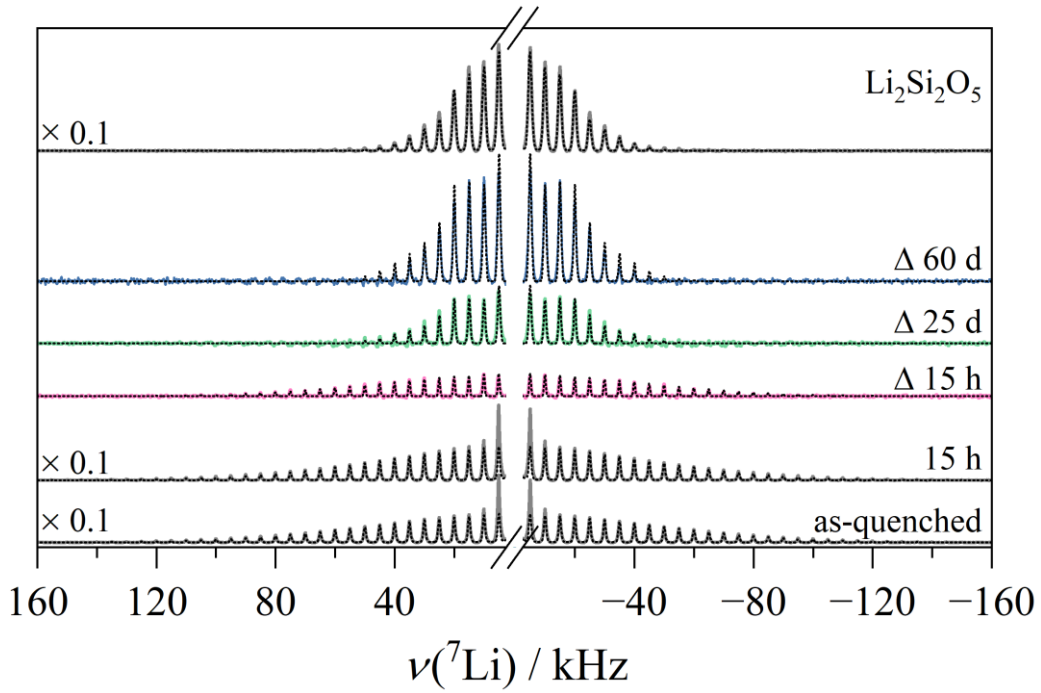

Figure 9: Experimental SATRAS difference spectra (colored curves) and their simulations (dotted curves). See text in section 3.7 for further details.

3.8 Final remarks

In line with the commonly observed characteristic of glasses exhibiting volume crystallization [48], the spatial modifier ion distribution in LS2 glass is already closely related to that in the crystalline state. It differs significantly from a random distribution, showing clear indications of clustering, as evidenced from second-moment measurements. Structural relaxation of LS2 glass caused by sub-T_g annealing produces significant changes in the local environment of the lithium ions, which manifest themselves in a moderate increase in the intermolecular ^{7}Li-^{7}Li dipole-dipole interaction strengths and a slight decrease of the average electric field gradients. With increasing treatment time, the corresponding NMR observables approach those of crystalline LS2, reflecting a tendency of the lithium ionic arrangements to become more “crystal-like”. This relaxation process is facilitated by the high ionic mobility of the lithium ions and appears to be completed after 15 h of treatment at 435 K. On the other hand, no changes in the silicate speciation are observable, neither by solid-state NMR nor by Raman spectroscopy. As the disproportionation equilibrium constant defined by eq. (1), K_3, is expected to decrease with decreasing fictive temperature, we expect that relaxation would also involve a readjustment of the Q^n species concentrations. Given the moderate difference between the fictive temperature of the as-quenched glass and the annealing temperature of 435 °C such readjustments will be minor, however, and may go undetected within the experimental error involved in the ^{29}Si MAS-NMR structural analysis. Furthermore, because of the low mobility of the silicate

species below T_g, it appears unlikely that this part of the relaxation process can be completed before crystal nucleation intervenes. Crystal nucleation is clearly indicated by the appearance of a sharp resonance near -91.5 ppm in the ^{29}Si MAS-NMR spectra, first observed after 40 days of thermal treatment at 435 °C, and by the appearance of a small fraction of ^{7}Li nuclei with significantly altered electric field gradient distributions, as indicated by the SATRAS difference spectroscopy. Again, the volume fraction of these nucleated crystals is too small to cause detectable changes in the silicate Q^n speciation of the surrounding glass matrix. The quantitative transformation of glassy lithium disilicate with its speciation of ~ 78 % Q^3 and 11% of Q^4 and Q^2 units to mostly-Q^3 will occur after much longer times at this temperature when the volume fraction of crystalline LS2 will significantly increase. The maximum growth rate of lithium disilicate has been determined to lie in the vicinity of 920 °C [49]. On crystallization, bond switching dynamics take place such that the shift in equilibrium (1) caused by the removal of Q^3 units via incorporation into the crystalline LS2 material will produce more Q^3 units from synproportionation of Q^2 and Q^4 units until the whole material is fully crystallized.

4. Conclusions

The present contribution develops a combined NMR and MD strategy to provide new atomic-level information about the structural organization of the lithium ions in LS2 glass and its evolution upon relaxation and crystal nucleation with sub-T_g annealing. The results confirm the previous hypothesis that the network modifier arrangements in homogeneously nucleating glasses are closely related to those in the isochemical crystals [48], and continuously approach each other during the relaxation process. The structural evolution of the lithium ions upon relaxation and nucleation can be followed using dipolar and quadrupolar ^{7}Li NMR observables extractable from interaction-selective solid state NMR experiments. While the present contribution is focused on lithium disilicate glass, the NMR strategy developed here will be generally applicable for investigating and monitoring the structural aspects of relaxation and nucleation of frozen supercooled ion-conducting liquids featuring suitable NMR nuclei (^{7}Li, ^{23}Na, ^{133}Cs) towards their ultimate fate of crystallization.

5. Acknowledgments

This work was supported by the São Paulo Research Foundation (FAPESP) under grant no. 2013/07793-6 (CEPID program). H.B. and A.G are grateful for the post-doctoral support received from FAPESP under grant numbers 2019/26399-3 and 2021/06370-0. HE (310870/2020-8) and EDZ (303886/2015-3) are grateful to CNPq for a Bolsa de Pesquisa Grant.

6. References

[1] R. Zallen, The physics of amorphous solids, John Wiley & Sons, 2008.
[2] R.H. Doremus, Glass Science (2nd ed.), VCH-Wiley, 1994.
[3] A.K. Varshneya, J.C. Mauro, Fundamentals of Inorganic Glasses (Third Edition), Elsevier, 2019.
[4] E.D. Zanotto, J.C. Mauro, The glassy state of matter: Its definition and ultimate fate, J. Non. Cryst. Solids 471 (2017) 490-495
[5] D. Holland, Y. Iqbal, P. James, B. Lee, Early stages of crystallisation of lithium disilicate glasses containing P_2O_5 – An NMR study, J. Non. Cryst. Solids 232-234 (1998) 140-146.
[6] R. Dupree, D. Holland, M. Mortuza, A MAS-NMR investigation of lithium silicate glasses and glass ceramics, J. Non. Cryst. Solids 116(2-3) (1990) 148-160.
[7] Y. Iqbal, W. Lee, D. Holland, P. James, Metastable phase formation in the early stage crystallisation of lithium disilicate glass, J. Non. Cryst. Solids 224(1) (1998) 1-16.
[8] R. Küchler, O. Kanert, T. Vereget, H. Jain, Effect of devitrification on ion motion in lithium-disilicate glass, J. Non. Cryst. Solids 353(41-43) (2007) 3940-3946.
[9] T. Fuss, A. Moguš-Milanković, C. Ray, C. Lesher, R. Youngman, D. Day, Ex situ XRD, TEM, IR, Raman and NMR spectroscopy of crystallization of lithium disilicate glass at high pressure, J. Non. Cryst. Solids 352(38-39) (2006) 4101-4111.
[10] D.J. Burkhard, G. Nachtegaal, Nucleation and growth behavior of lithium disilicate at pressures to 0.5 GPa investigated by NMR spectroscopy, J. Non. Cryst. Solids 209(3) (1997) 299-304.
[11] J.G. Longstaffe, U. Werner-Zwanziger, J.F. Schneider, M.L. Nascimento, E.D. Zanotto, J.W. Zwanziger, Intermediate-range order of alkali disilicate glasses and its relation to the devitrification mechanism, J. Phys. Chem. **C** 112(15) (2008) 6151-6159.
[12] C. Schröder, M.d.O.C. Villas-Boas, F.C. Serbena, E.D. Zanotto, H. Eckert, Monitoring crystallization in lithium silicate glass-ceramics using $^{7}Li \rightarrow ^{29}Si$ cross-polarization NMR, J. Non. Cryst. Solids 405 (2014) 163-169.
[13] C. Bischoff, H. Eckert, E. Apel, V.M. Rheinberger, W. Höland, Phase evolution in lithium disilicate glass–ceramics based on non-stoichiometric compositions of a multi-component system: structural studies by ^{29}Si single and double resonance solid state NMR, Phys. Chem. Chem. Phys. 13(10) (2011) 4540-4551.
[14] J. Hendrickson, P. Bray, Nuclear magnetic resonance studies of ^{7}Li ionic motion in alkali silicate and borate glasses, J. Chem. Phys. 61(7) (1974) 2754-2764.
[15] P. Soares Jr, E. Zanotto, V. Fokin, H. Jain, TEM and XRD study of early crystallization of lithium disilicate glasses, J. Non. Cryst. Solids 331(1-3) (2003) 217-227.
[16] M.L.F. Nascimento, V.M. Fokin, E.D. Zanotto, A.S. Abyzov, Dynamic processes in a silicate liquid from above melting to below the glass transition, J. Chem. Phys. 135(19) (2011) 194703.
[17] A.P. Thompson, H.M. Aktulga, R. Berger, D.S. Bolintineanu, W.M. Brown, P.S. Crozier, P.J. in't Veld, A. Kohlmeyer, S.G. Moore, T.D. Nguyen, LAMMPS-a flexible simulation tool for particle-based materials modeling at the atomic, meso, and continuum scales, Comput. Phys. Commun. 271 (2022) 108171.
[18] S. Plimpton, Fast parallel algorithms for short-range molecular dynamics, J. Comput. Phys. 117(1) (1995) 1-19.
[19] A. Pedone, G. Malavasi, M.C. Menziani, A.N. Cormack, U. Segre, A new self-consistent empirical interatomic potential model for oxides, silicates, and silica-based glasses, J. Phys. Chem. **B** 110(24) (2006) 11780-11795.
[20] P.P. Ewald, Die Berechnung optischer und elektrostatischer Gitterpotentiale, Ann. Phys. 369(3) (1921) 253-287.
[21] S. Nosé, A unified formulation of the constant temperature molecular dynamics methods, J. Chem. Phys. 81(1) (1984) 511-519.

[22] W. Shinoda, M. Shiga, M. Mikami, Rapid estimation of elastic constants by molecular dynamics simulation under constant stress, Phys. Rev. B 69(13) (2004) 134103.
[23] A. Stukowski, Visualization and analysis of atomistic simulation data with OVITO–the Open Visualization Tool, Modell. Simul. Mater. Sci. Eng. 18(1) (2009) 015012.
[24] C. Jäger, W. Müller-Warmuth, C. Mundus, L. van Wüllen, ^{27}Al MAS-NMR spectroscopy of glasses: new facilities by application of 'SATRAS', J. Non. Cryst. Solids 149(3) (1992) 209-217.
[25] G. Czjzek, J. Fink, F. Götz, H. Schmidt, J.M.D. Coey, J.P. Rebouillat, A. Liénard, Atomic coordination and the distribution of electric field gradients in amorphous solids, Phys. Rev. B 23(6) (1981) 2513-2530.
[26] S.G.J. van Meerten, W.M.J. Franssen, A.P.M. Kentgens, ssNake: A cross-platform open-source NMR data processing and fitting application, J. Mag. Res. 301 (2019) 56-66.
[27] M. Bak, J.T. Rasmussen, N.C. Nielsen, SIMPSON: A General Simulation Program for Solid-State NMR Spectroscopy, J. Mag. Res. 147(2) (2000) 296-330.
[28] H. Bradtmüller, Structure-property Relationships in Glasses and Glass-ceramics Characterized by Solid-state NMR Spectroscopy, Westfälische Wilhelms-Universität, Münster, 2019.
[29] J. Haase, E. Oldfield, Spin-Echo Behavior of Nonintegral-Spin Quadrupolar Nuclei in Inorganic Solids, J. Magn. Reson., Ser. A 101(1) (1993) 30-40.
[30] D. Lathrop, D. Franke, R. Maxwell, T. Tepe, R. Flesher, Z. Zhang, H. Eckert, Dipolar ^{31}P NMR spectroscopy of crystalline inorganic phosphorus compounds, Solid State Nucl. Mag. Reson. 1(2) (1992) 73-83.
[31] B. Gee, H. Eckert, ^{23}Na nuclear magnetic resonance spin echo decay spectroscopy of sodium silicate glasses and crystalline model compounds, Solid State Nucl. Mag. Reson. 5(1) (1995) 113-122.
[32] J.H. Van Vleck, The dipolar broadening of magnetic resonance lines in crystals, Phys. Rev. 74(9) (1948) 1168.
[33] R. Artiaga, J. López-Beceiro, J. Tarrío-Saavedra, C. Gracia-Fernández, S. Naya, J.L. Mier, Estimating the reversing and non-reversing heat flow from standard DSC curves in the glass transition region, J. Chemom. 25(6) (2011) 287-294.
[34] R.F. Lancelotti, A.C.M. Rodrigues, E.D. Zanotto, Structural relaxation dynamics of a silicate glass via three properties, J. Am. Ceram. Soc. (To be submitted).
[35] O.N. Koroleva, T.N. Ivanova, Raman spectroscopy of the structures of Li_2O-SiO_2 and Li_2O-GeO_2 melts, Russian Metallurgy (Metally) 2014(2) (2014) 140-146.
[36] S. Jurca, H. Chen, S. Sen, Structural, shear and volume relaxation in a commercial float glass during aging, J. Non. Cryst. Solids 589 (2022) 121650.
[37] R. Al-Mukadam, J. Deubener, Heterogeneous crystal nucleation of supercooled lithium disilicate melt in glassy carbon containers, J. Non. Cryst. Solids 571 (2021) 121068.
[38] V. Devarajan, H. Shurvell, Vibrational spectra and normal coordinate analysis of crystalline lithium metasilicate, Canadian Journal of Chemistry 55(13) (1977) 2559-2563.
[39] J. Emerson, P. Stallworth, P.J. Bray, High-field ^{29}Si NMR studies of alkali silicate glasses, J. Non. Cryst. Solids 113(2-3) (1989) 253-259.
[40] W. Sun, V. Dierolf, H. Jain, Molecular dynamics simulation of the effect of cooling rate on the structure and properties of lithium disilicate glass, J. Non. Cryst. Solids 569 (2021) 120991.
[41] J.C. Mauro, Y. Yue, A.J. Ellison, P.K. Gupta, D.C. Allan, Viscosity of glass-forming liquids, Proceedings of the National Academy of Sciences 106(47) (2009) 19780-19784.
[42] F. Lodesani, M.C. Menziani, K. Maeda, Y. Takato, S. Urata, A. Pedone, Disclosing crystal nucleation mechanism in lithium disilicate glass through molecular dynamics simulations and free-energy calculations, Sci. Rep. 10(1) (2020) 17867.
[43] J. Zhao, P.H. Gaskell, M.M. Cluckie, A.K. Soper, A neutron diffraction, isotopic substitution study of the structure of $Li_2O{\cdot}2SiO_2$ glass, J. Non. Cryst. Solids 232-234 (1998) 721-727.

[44] F. Liebau, Untersuchungen an Schichtsilikaten des Formeltyps Am $(Si_2O_5)_n$. I. Die Kristallstruktur der Zimmertemperaturform des $Li_2Si_2O_5$, Acta Crystallogr. 14(4) (1961) 389-395.
[45] B.H.W.S. de Jong, H.T.J. Super, A.L. Spek, N. Veldman, G. Nachtegaal, J.C. Fischer, Mixed Alkali Systems: Structure and ^{29}Si MAS NMR of $Li_2Si_2O_5$ and $K_2Si_2O_5$, Acta Crystallogr. B Struct. Sci. 54(5) (1998) 568-577.
[46] R.I. Smith, R.A. Howie, A.R. West, A. Aragon-Pina, M.E. Villafuerte-Castrejon, The structure of metastable lithium disilicate, $Li_2Si_2O_5$, Acta Crystallogr. C Struct. Chem. 46(3) (1990) 363-365.
[47] A. Abragam, The principles of nuclear magnetism, Oxford university press, 1961.
[48] E.D. Zanotto, J.E. Tsuchida, J.F. Schneider, H. Eckert, Thirty-year quest for structure–nucleation relationships in oxide glasses, Int. Mater. Rev. 60(7) (2015) 376-391.
[49] K. Matusita, M. Tashiro, Rate Of Crystal Growth In Li_2O-$2SiO_2$ Glass, J. Ceram. Soc. Jap. 81(11) (1973) 500-506